PHOTONICS Research

Tuning the second-harmonic generation in AlGaAs nanodimers via non-radiative state optimization [Invited]

Davide Rocco,[1,*] Valerio F. Gili,[2] Lavinia Ghirardini,[3] Luca Carletti,[1] Ivan Favero,[2] Andrea Locatelli,[1,4] Giuseppe Marino,[2,5] Dragomir N. Neshev,[5] Michele Celebrano,[3] Marco Finazzi,[3] Giuseppe Leo,[2] and Costantino De Angelis[1,4]

[1]Department of Information Engineering, University of Brescia, Via Branze 38, Brescia 25123, Italy
[2]Matériaux et Phénomènes Quantiques, Université Paris Diderot, CNRS UMR 7162, 10 rue A. Domon et L. Duquet, 75013 Paris, France
[3]Department of Physics, Politecnico di Milano, Piazza Leonardo Da Vinci 32, Milano 20133, Italy
[4]National Institute of Optics (INO), Via Branze 45, Brescia 25123, Italy
[5]Nonlinear Physics Centre, Research School of Physics and Engineering, The Australian National University, Canberra, ACT 2601, Australia
*Corresponding author: d.rocco003@unibs.it

Received 6 November 2017; revised 15 January 2018; accepted 19 January 2018; posted 19 January 2018 (Doc. ID 312427); published 11 April 2018

Dielectric nanocavities are emerging as a versatile and powerful tool for the linear and nonlinear manipulation of light at the nanoscale. In this work, we exploit the effective coupling of electric and toroidal modes in AlGaAs nanodimers to locally enhance both electric and magnetic fields while minimizing the optical scattering, thereby optimizing their second-harmonic generation efficiency with respect to the case of a single isolated nanodisk. We also demonstrate that proper near-field coupling can provide further degrees of freedom to control the polarization state and the radiation diagram of the second-harmonic field.

OCIS codes: (190.5890) Scattering, stimulated; (190.4360) Nonlinear optics, devices; (190.4400) Nonlinear optics, materials; (290.5825) Scattering theory.

https://doi.org/10.1364/PRJ.6.0000B6

1. INTRODUCTION

Dielectric nanoantennas have recently gained increasing interest for nonlinear optics applications due to their large nonlinearities and extremely low dissipative losses in the optical regime compared to metals [1,2]. Single nanostructures based on high-refractive index materials have already demonstrated unique second- and third-order nonlinear optical properties [3–9]. While in metal-based nanoantennas the electric field is strongly confined to the surface, in dielectric nanoparticles the electric field of the resonant modes establishes within their volume, hence strongly enhancing intracavity light–matter interactions. In view of these results, metal-less nonlinear nanophotonics is expected to become of paramount importance, also because the optical response of high-permittivity dielectric nanoparticles in a low-refractive index background exhibits negligible ohmic losses and extremely narrow magnetic and electric multipole resonances in both the visible and near-infrared regions of the electromagnetic spectrum [10–13]. These optical properties can be easily tailored, hence enabling applications in many fields, ranging from spectroscopy and sensing to photovoltaic devices and quantum optics. In the long term, dielectric nanoantennas and metasurfaces exploiting second-order nonlinear effects are expected to provide a platform with an unprecedented level of efficiency and control over both polarization and the spatial and frequency properties of the photons generated by either sum frequency (SFG) or difference frequency generation (DFG), or by spontaneous parametric downconversion (SPDC) [14]. In this framework, the engineering of the polarization state and the radiation pattern of the nonlinearly generated beams plays a key role, and promising results have been reported using either single or coupled nanoantennas [15–19]. In comparison with single nanostructures, nanodimers formed by two coupled nanocavities [20–22] offer further tunability and engineering capabilities for complete control of the properties of the nonlinearly generated beams. One of them is the dependence of the optical response on the linear polarization state of the impinging light with two basic configurations: light polarized parallel and perpendicular to the dimer axis. Moreover, the strong coupling between the induced dipoles at the fundamental frequency (FF) affects the second-harmonic generation (SHG) process. In this work, we study the polarization properties and the directionality features

in the process of degenerate SFG (i.e., SHG) in AlGaAs nanodimers grown on aluminum oxide. The paper is organized as follows: in Section 2, we illustrate the key properties of the near- and far-field linear scattering of single cylinders and dimers; in Section 3, we describe theoretically and experimentally the polarization state and the radiation pattern of optical beams generated through SHG by bulk $\chi^{(2)}$ in the dielectric dimers. Our results show that closely packed AlGaAs nanoantennas allow one to add further degrees of freedom for nonlinear light manipulation, enabling emission modulation at the nanoscale. This engineering is also accompanied by an increase in the overall emitted SHG, which is a fundamental feature in view of realizing efficient nonlinear metasurfaces for the complete control of light generated by nanoantennas through second-order nonlinear processes.

2. LINEAR SCATTERING PROPERTIES OF SINGLE AND DIMER NANOCYLINDERS

The single and dimer cylindric structures used here as nanoantennas for SHG were fabricated on an aluminum oxide (AlOx) substrate via electron-beam lithography. Our samples were grown by molecular beam epitaxy on a non-intentionally doped [100] GaAs wafer, with a 400 nm layer of $Al_{0.18}Ga_{0.82}As$ on top of an $Al_{0.98}Ga_{0.02}As$ substrate to be oxidized at a later stage. Before electron-beam lithography, a 3 nm layer of SiO is deposited on the surface to improve adhesion of the negative-tone HSQ resist. After development in AZ400K, the SiO layer is removed through CHF_3 reactive-ion etching. The dimer patterns are then defined with $SiCl_4$-assisted inductively coupled plasma etching (ICP). The latter continues for about 150 nm in the Al-rich layer so as to clearly define the gap between pillars. The fabrication procedure is concluded by selective oxidation at 390°C for 30 min of the Al-rich layer revealed by ICP. The final result of the fabrication process is: $Al_{0.18}Ga_{0.82}As$ nanostructures on AlOx 1-μm-thick substrate resting on a non-intentionally doped GaAs wafer, as already reported in Ref. [7]. We first numerically and experimentally analyze the extinction spectrum of the fabricated samples to explore their linear response. We simulate the scattering characteristics of $Al_{0.18}Ga_{0.82}As$ cylinders of a 400 nm height and a radius between 280 and 360 nm at near-IR wavelengths by using full-vectorial electromagnetic simulations implemented using the finite element method in COMSOL. The incident light is either a plane wave or a focused Gaussian beam at a wavelength of 1550 nm with a wave vector parallel to the cylinder axis, and the electric field is polarized along the x axis. For dispersion of the refractive index of $Al_{0.18}Ga_{0.82}As$ we use the analytical model proposed in Ref. [23]. To gain a deeper physical understanding of the modes excited in the nanocylinder structure, we resorted to the multipolar expansion in Cartesian coordinates of the displacement currents induced by the incident electric field [24]. We thus evaluated the terms p, m, t, Q_e, and Q_m, which refer to the electric dipole, magnetic dipole, toroidal dipole, electric quadrupole, and magnetic quadrupole moments, respectively. Figure 1(a) shows the calculated extinction efficiency and the optical contrast measurement in a single nanocylinder with a radius between 280 and 360 nm and a height of 400 nm. For the considered wavelength range the absorption of the AlGaAs is negligible. Thus, the extinction corresponds to the scattered power, which is normalized to the nanocylinder geometrical cross section and incident intensity. We measure the optical contrast as the relative reflected intensity from the sample at the fundamental wavelength: $(I_{\text{cylinder}} - I_{\text{ref}})/I_{\text{ref}} = \Delta I/I_{\text{ref}}$, where I_{ref} is

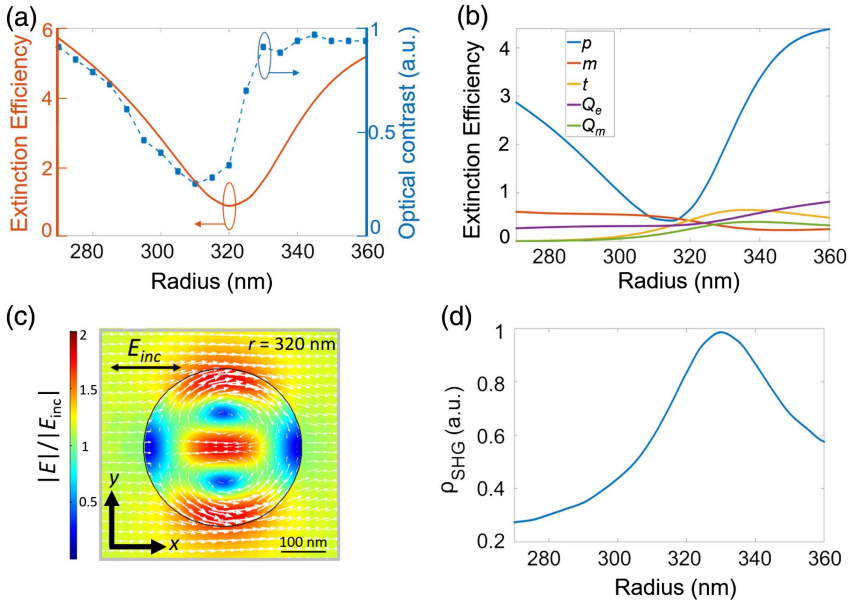

Fig. 1. (a) Extinction efficiency of the isolated cylinder versus the radius of its section: the continuous (dashed) line refers to modeling (experimental data); (b) extinction efficiency decomposed in electric dipole p, magnetic dipole m, toroidal dipole t, electric quadrupole Q_e, and magnetic quadrupole Q_m contributions. (c) Electric field enhancement for a nanocylinder with radius 320 nm. The white arrows indicate the electric field vector (in-plane components). (d) Magnitude of the volume integral of the normalized nonlinear current density ρ_{SHG} inside the cylinder as a function of the radius.

the reference reflected intensity from the substrate. ΔI corresponds to the scattering measured from the cylinder. We can observe that the extinction goes through a minimum for a radius of 320 nm. From the calculated multipolar moments [see Fig. 1(b)], we can also appreciate that such dip is mainly dictated by the electric dipole contribution. It is worth noting, however, that for this radius the electric dipole and toroidal dipole moments are both excited. We recall that the electric anapole condition can be viewed as a superimposition of electric and toroidal moments of equal amplitude and with a phase difference equal to π. The fields radiated by these multipole moments interfere destructively in the far-field region, which results in a zero-scattering condition that is the fingerprint of the anapole condition. In the fabricated cylinder the almost complete destructive interference between the far-field radiation emitted by the electric and toroidal dipoles is perturbed by the higher order multipole moments (electric and magnetic quadrupoles), which prevent the anapole condition to be fully satisfied.

This can be noticed by the fact that the efficiency is not exactly zero for $r = 320$ nm. Indeed, for this specific radius, the electric field distribution inside the nanocylinder resembles the typical anapole resonance [Fig. 1(c)] [25]. We can thus assume that the additional multipole moments are negligible for our purpose. The use of an anapole state for enhancing nonlinear effects has already been reported in the literature [26] and deserves a deeper analysis here.

Therefore, to assess the potential of our nanoantenna for SHG, we evaluate

$$|\rho_{\mathrm{SHG}}| = \left|2\omega\varepsilon_0 \sum_{i,j,k} \int \chi^{(2)}_{ijk} E^{\omega}_j E^{\omega}_k \mathrm{d}V\right|, \tag{1}$$

the volume integral of the nonlinear current density inside the AlGaAs cylinder as a function of the radius.

Since AlGaAs has a zinc blende crystalline structure, the only non-vanishing terms of the nonlinear susceptibility tensor $\chi^{(2)}_{ijk}$ are the ones with $i \neq j \neq k$. As shown in Fig. 1(d), the normalized ρ_{SHG} has a maximum that is clearly associated with the dip in the scattering behavior of Fig. 1(a). The 10 nm shift in wavelength between the two features might be possibly attributed to the presence of multipole moments other than the electric dipole and toroidal ones.

Let us now consider a nanodimer structure formed by two identical cylinders with a 30 nm gap, as shown in the scanning-electron-microscope image in Fig. 2(a). The two cylinders have radii in the range 270–360 nm, and the gap between them has been chosen to guarantee a strong coupling. We first focused our attention to the linear scattering behavior of the nanodimer for two incident polarizations of the electric field, i.e., along (x) or across (y) the dimer axis [see Fig. 2(b)].

In this preliminary stage we focus our attention on the excitation conditions of the anapole-like state in the dimer under different incident light polarizations. Because of maximization of the internal energy, we expect that the SHG efficiency will be enhanced at this condition. The multipolar moments excited inside the nanodimer can be obtained by integrating the induced currents over the whole volume [24].

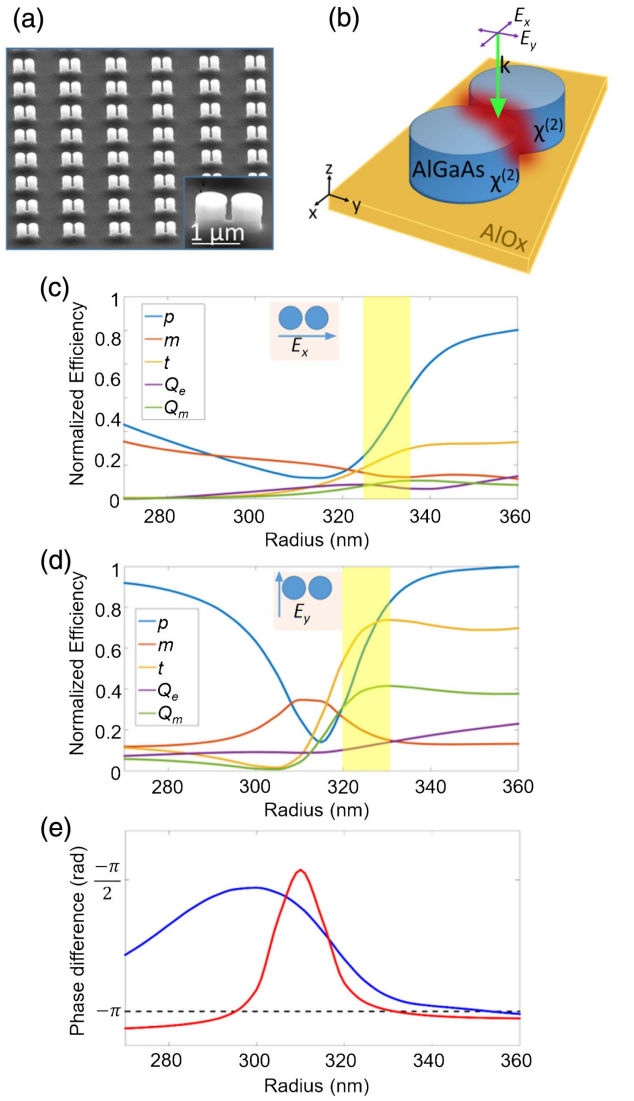

Fig. 2. AlGaAs-on-AlOx nanodimers. (a) SEM image of a part of the array. The principal axis of the dimer is oriented parallel to the [100] direction of the AlGaAs crystal. (b) Pictorial view of the proposed structure. Calculated Cartesian decomposition of the dimer photonic modes in the case of light linearly polarized either along (c) the x axis or (d) the y axis for different dimer radii at $\lambda = 1550$ nm. (e) Phase difference between p and t multipoles in the case of incident light polarized along the x (blue curve) or the y axis (red curve). A black dashed line corresponding to $-\pi$ is plotted as a reference.

Such multipolar moments, reported in Figs. 2(c) and 2(d) versus the radius for the two different incident polarizations, show two main features: 1) the toroidal dipole contribution to the total scattering becomes essential for large particles and its contribution to the scattered field must be considered; 2) for small particles the contribution of the electric dipole is dominant, while the toroidal moment is negligible. Moreover, for x-polarized light the electric and toroidal dipoles dominate for $r > 330$ nm, while they have a similar magnitude [yellow region in Fig. 2(c)] and a phase difference close to $-\pi$ [Fig. 2(e)] for $r = 335$ nm, where they almost satisfy the

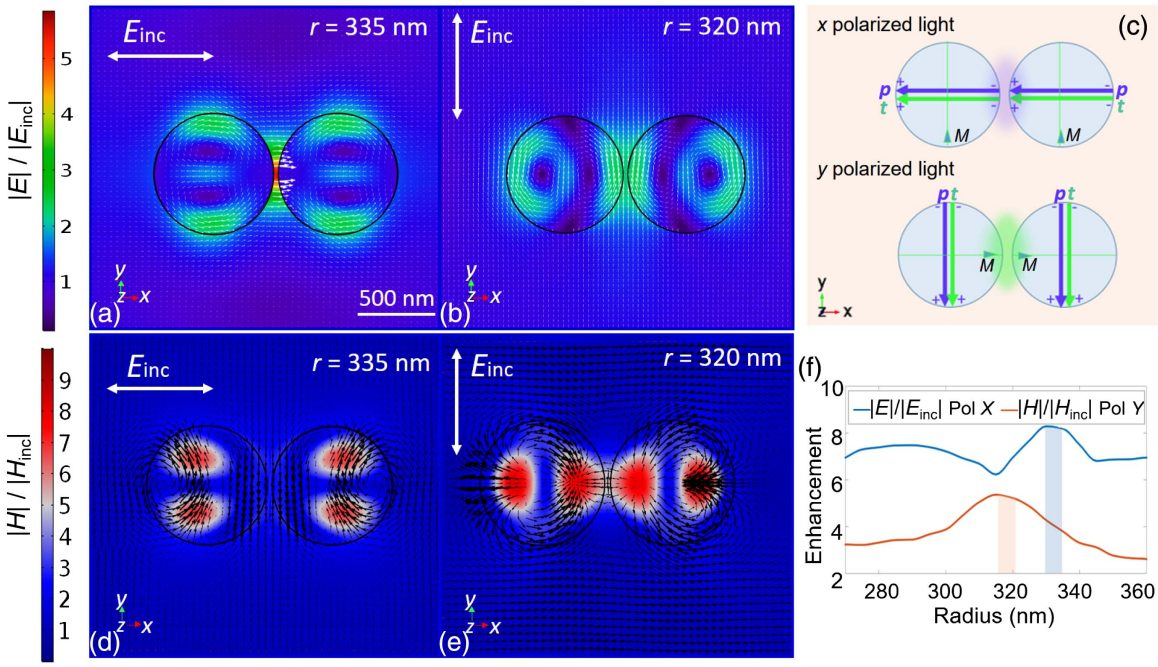

Fig. 3. (a) Electric–magnetic field distribution in the x–y plane at the fundamental wavelength in the dimer structure for the two incident (inc) polarizations, as indicated by the white arrows: for a dimer with (a), (d) a radius of 335 nm and (b), (e) with a radius of 320 nm; in (a) and (b) the height is 200 nm; in (d) and (e) it is 300 nm. (c) Schematic description of the coupling mechanism in the dimer for the two orthogonal incident polarizations: p indicates the electric dipole, t is the toroidal dipole, and M is the magnetic field loop. (f) Electric and magnetic field enhancement as a function of the dimer radius for the x (blue curve) and y (orange curve) incident polarizations.

anapole condition. Instead, for y-polarized light, two intersections between the electric dipole and toroidal dipole contributions are predicted around 315 nm and around 325 nm [yellow region in Fig. 2(d)], but only the latter corresponds to a phase difference close to $-\pi$ [Fig. 2(e)]; in addition, for $r < 320$ nm the contribution of the magnetic dipole is not negligible, while for larger radii other higher order contributions appear, hampering the excitation of the anapole mode.

The simulated electric and magnetic near-field profiles for the considered radii ($r = 335$ nm and $r = 320$ nm) are shown in Fig. 3. An electric hotspot can be clearly observed between the two particles for both incident polarizations [see Figs. 3(a) and 3(b)]. The electric field shows a stronger enhancement (larger than a factor 8) in the gap for the case of x-polarized light than for the case of y-polarized light (~2.5). For x-polarized light, this is due to the coupling of induced electric dipoles in the cylinders [22]. Instead, for y-polarized light, the electric field hotspot between the cylinders can be interpreted as a consequence of coupling between the induced toroidal dipoles. A schematic of this mechanism is plotted in Fig. 3(c), assuming that the cylinders are at the exact anapole condition and thus support just the electric and toroidal dipole moments. The toroidal dipole moment is associated with a circulating magnetic field M accompanied by an electric poloidal current distribution. On the other hand, the magnetic field has a higher enhancement (>5) for y-polarized light compared to x-polarized light (~2.5), as shown in Figs. 3(d) and 3(e). The enhancement inside the gap is lower than that inside the nanoparticles (>10) but still high enough to be accessible for near-field measurements or to be used for enhancing the radiation from localized emitters [27,28]. The electric and magnetic field enhancement as a function of the dimer radius is reported in Fig. 3(f) for x- and y-polarized light, respectively. Note that the negligible field distribution outside the single cylinder [Fig. 1(c)] clarifies the role of the dimer structure for the above-mentioned field enhancement.

3. SHG FROM AlGaAs DIMERS

Using both numerical simulations and experimental findings, we have investigated the SHG process in the dimers, whose relevant linear features were introduced in Section 2. In the numerical simulations we use the nonlinear polarization associated with the $\chi^{(2)}$ tensor of $Al_{0.18}Ga_{0.82}As$ as a source in the frequency domain. We thus take into account, as already done in Ref. [7], only the volume nonlinear susceptibility in the theoretical calculations. More precisely, as reported in Ref. [29], we solve the linear electromagnetic problem at the FF and then the problem at the second harmonic (SH) using the previously computed FF fields to determine the current density which forces the evolution of the SH fields. Figure 4(a) shows the calculated SHG efficiency (ratio of the emitted SHG over the pump power incident on the nanostructure, [6]) in the case of x and y incident polarizations of the electric field of the pump beam. Our numerical calculations predict a total SHG efficiency exceeding 4×10^{-6} using a pump intensity of 1.6 GW/cm^2 with wavelength equal to 1.55 μm.

For light polarized parallel to the dimer axis (i.e., x polarized), this peak is reached for $r = 335$ nm, while for light polarized orthogonal to the dimer axis (i.e., y polarized), the maximum is obtained for $r = 320$ nm. It is worth noting that

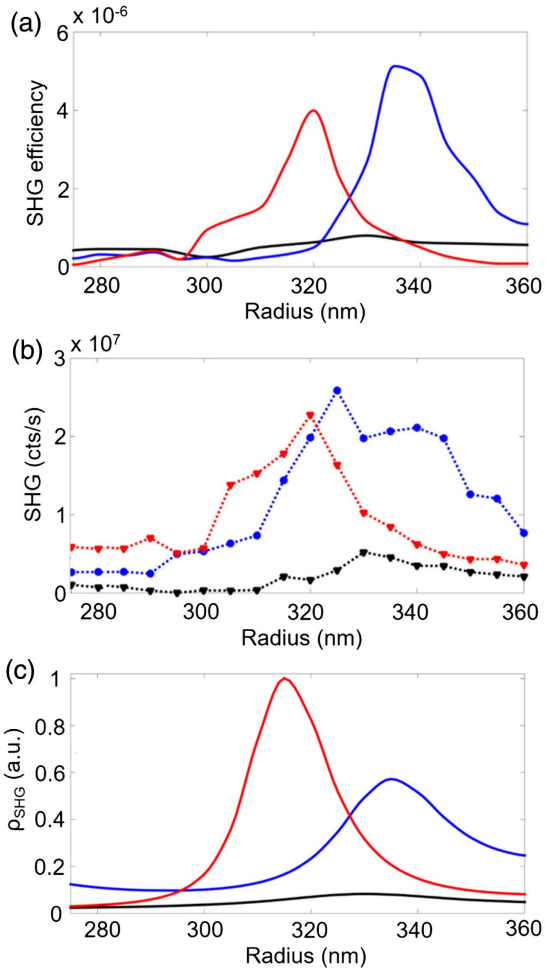

Fig. 4. (a) Numerical calculations of the SH efficiency for *x*-polarized pump beam (blue line) and *y*-polarized pump beam (red line) as a function of cylinder radius with respect to the SHG of the single cylinder (black line). (b) Measured SHG for the dimer structure as a function of radius for two pump polarizations: along the *x* axis (blue curve) and along the *y* axis (red curve). The black line represents the measured SHG for the single cylinder structure. (c) Calculated volume integral of the nonlinear polarization in the isolated cylinder (black line) and in the dimer for *x*- (blue line) and *y*- (red line) polarized pump beams.

the SHG efficiency, for both incident polarizations, is about 5 times higher than that of a single cylinder of the same radius, which corresponds to an enhancement of more than a factor 20 in SHG power. This increase can be explained by the coupling between the electric dipoles (in each cylinder that forms the dimer) for the *x*-polarized light and between the toroidal dipoles for the *y*-polarized light. Moreover, we observe that the dimer SHG peaks are at the same radius for which a maximum local enhancement of both the electric and the magnetic fields is observed in the gap region at the fundamental wavelength [see Figs. 3(f) and 4(a)]. This feature could be useful in sensing applications where changes in the gap region will be reflected in strong perturbations of the SH signal, while transparent at the fundamental frequency, due to the anapole state.

We experimentally investigated the nonlinear emission from each individual nanodimer by means of a commercial WITEC microscope operating in confocal reflection mode and using a high-numerical-aperture (NA) air objective (Olympus, 0.85 NA). The light source employed is an Er-doped fiber laser centered at 1550 nm with a pulse duration of 10 ps. The use of a polarization maintaining fiber ensures that the light impinging on the sample is linearly polarized. The size of the waist radius is about 1 μm, while the peak pump intensity at the focus is about 1 GW/cm^2. A short-pass filter at 800 nm and a long-pass filter at 600 nm are inserted in the collection path to remove any possible photoluminescence from the substrate and the third-harmonic signal from the cylinders. The dependence of the experimentally detected SHG on the radius size of the nanodimers is reported in Fig. 4(b) for the different incident polarizations. The plotted values are subtracted by the background coming from the AlOx substrate, which is, however, about 3 orders of magnitude weaker than the signal from the dimers. Two broad maxima can be identified in the emission behavior: at $r \sim 330$–340 nm for *x*-polarized pump light and at $r = 320$ nm for *y*-polarized pump light. These results are in excellent agreement both with the calculated efficiency plots [Fig. 4(a)] and with the volume integral of the nonlinear current density that is reported in Fig. 4(c): the maxima of the nonlinear polarization are in the same position of the SHG peaks and the ones related to the dimers (for both incident polarizations) are about 1 order of magnitude larger than the efficiency of the isolated cylinder. The results in Fig. 4(b) show shoulders that are not predicted by the theoretical ρ_{SHG}. The latter considers only the pump fields, so the mismatch is due to the contribution of SH modes. Additionally, this comparison gives the magnitude (small modulation) of the SH modal contribution. The presence of two different SHG maxima both in Figs. 4(a) and 4(b) suggests the existence of an additional degree of freedom that allows one to modulate the SHG by tuning with the polarization of the pump light. This feature can disclose new design approaches in building anisotropic nonlinear metasurfaces based on high-permittivity semiconductors. This key enabling feature becomes even more evident if one analyzes the radiation pattern of a dimer. In Figs. 5(a) and 5(b) we show, respectively, the SHG radiation pattern acquired on cylinders with radius 335 nm (for the *x*-polarized pump) and radius 320 nm (for the *y*-polarized pump). The upper panels show the results obtained from the numerical modeling, while the lower ones show the corresponding experimental data; in both cases the back focal plane images are obtained from the light collected through a numerical aperture of 0.85. The deviations between the calculated and measured radiation pattern for the cross-polarized case in Fig. 5(b) may be due to differences between the nominal and experimental value of the NA. Moreover, small fabrication defects regarding the radius and the gap between the cylinders can alter the SH radiation pattern in a significant way. A complete SH multipole decomposition would give the possibility to describe the differences between the radiation diagrams shown in Fig. 5.

Moreover, the good agreement between theory and experiment allows us to validate our modeling and our assumptions

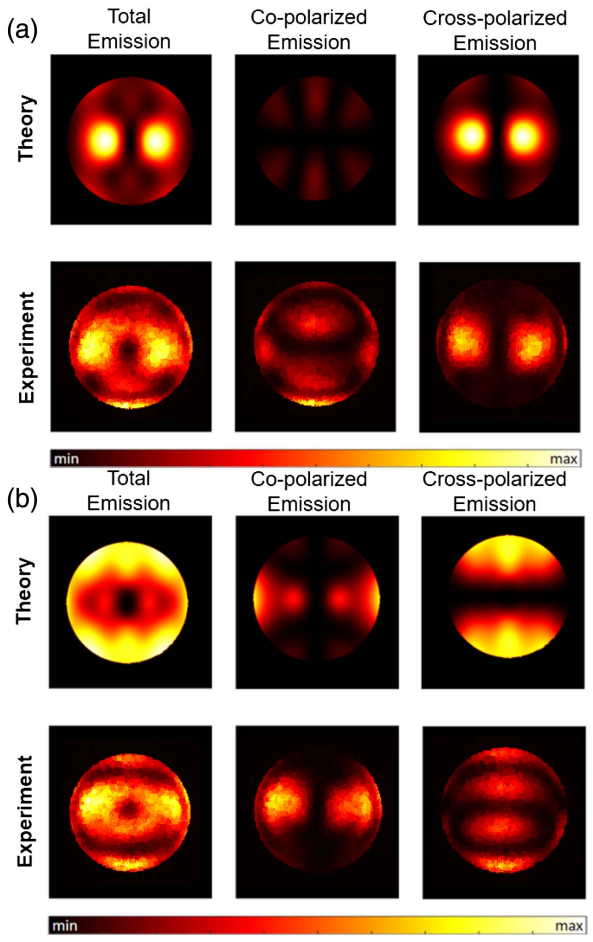

Fig. 5. Simulated (top) and experimentally obtained (bottom) SH emission patterns decomposed in co-polarized and cross-polarized (with respect to the pump beam) contributions for the dimer structure with $r = 335$ nm [(a) x-polarized pump] and with $r = 320$ nm [(b) y-polarized pump].

and to further unveil the physics of the nonlinear effects in a nanoscale AlGaAs integrated platform. The proposed structure can be a promising candidate for the realization of metasurfaces with efficient control over the polarization, and the spatial and frequency properties of photons generated by second-order nonlinear optical processes.

4. CONCLUSIONS

In conclusion, after discussing the linear optical properties of dielectric nanodimers, we have studied how the coupling between induced dipoles at the fundamental wavelength affects the process of SHG. Our results provide a deeper insight into the fundamental mechanisms of these resonators near the anapole scattering condition, showing the potential of high-refractive-index nanodimers in the nonlinear generation and control of light at the nanoscale. Moving from AlGaAs single nanoantennas to nanodimers adds a degree of freedom to the nonlinear light manipulation, resulting in efficient and tunable SHG. New avenues are now open for low-loss nanophotonics in the optical regime, with an important step toward the development of tunable nonlinear metasurfaces.

Funding. Australian Research Council (ARC); Education, Audiovisual and Culture Executive Agency (EACEA) (5659/002-001); SATT IdF-InnovUniversité Sorbonne (Double Culture—PhD program).

REFERENCES

1. A. I. Kuznetsov, A. Miroshnichenko, M. L. Brongersma, Y. S. Kivshar, and B. Luk'yanchuk, "Optically resonant dielectric nanostructures," Science **354**, aag2472 (2016).
2. I. Staude and J. Schilling, "Metamaterial-inspired silicon nanophotonics," Nat. Photonics **11**, 274–284 (2017).
3. M. R. Shcherbakov, D. N. Neshev, B. Hopkins, A. S. Shorokhov, I. Staude, E. V. Melik-Gaykazyan, M. Decker, A. A. Ezhov, A. E. Miroshnichenko, I. Brener, A. A. Fedyanin, and Y. S. Kivshar, "Enhanced third-harmonic generation in silicon nanoparticles driven by magnetic response," Nano Lett. **14**, 6488–6492 (2014).
4. M. R. Shcherbakov, A. S. Shorokhov, D. N. Neshev, B. Hopkins, I. Staude, E. V. Melik-Gaykazyan, A. A. Ezhov, A. E. Miroshnichenko, I. Brener, A. A. Fedyanin, and Y. S. Kivshar, "Nonlinear interference and tailorable third-harmonic generation from dielectric oligomers," ACS Photon. **2**, 578–582 (2015).
5. A. S. Shorokhov, E. V. Melik-Gaykazyan, D. A. Smirnova, B. Hopkins, K. E. Chong, D.-Y. Choi, M. R. Shcherbakov, A. E. Miroshnichenko, D. N. Neshev, A. A. Fedyanin, and Y. S. Kivshar, "Multifold enhancement of third-harmonic generation in dielectric nanoparticles driven by magnetic Fano resonances," Nano Lett. **16**, 4857–4861 (2016).
6. L. Carletti, A. Locatelli, O. Stepanenko, G. Leo, and C. De Angelis, "Enhanced second-harmonic generation from magnetic resonance in AlGaAs nanoantennas," Opt. Express **23**, 26544–26550 (2015).
7. V. F. Gili, L. Carletti, A. Locatelli, D. Rocco, M. Finazzi, L. Ghirardini, I. Favero, C. Gomez, A. Lemaître, M. Celebrano, C. De Angelis, and G. Leo, "Monolithic AlGaAs second-harmonic nanoantennas," Opt. Express **24**, 15965–15971 (2016).
8. S. Liu, M. B. Sinclair, S. Saravi, G. A. Keler, Y. Yang, J. Reno, F. Setzpfandt, I. Stause, T. Pertsch, and I. Brener, "Resonantly enhanced second-harmonic generation using III-V semiconductor all-dielectric metasurfaces," Nano Lett. **16**, 5426–5432 (2016).
9. R. Camacho-Morales, M. Rahmani, S. Kruk, L. Wang, L. Xu, D. A. Smirnova, A. S. Solntsev, A. Miroshnichenko, H. H. Tan, F. Karouta, S. Naureen, K. Vora, L. Carletti, C. De Angelis, C. Jagadish, Y. S. Kivshar, and D. N. Neshev, "Nonlinear generation of vector beams from AlGaAs nanoantennas," Nano Lett. **16**, 7191–7197 (2016).
10. H. Linnenbank, Y. Grynko, J. Förstner, and S. Linden, "Second harmonic generation spectroscopy on hybrid plasmonic/dielectric nanoantennas," Light Sci. Appl. **5**, e16013 (2016).
11. A. E. Krasnok, A. E. Miroshnichenko, P. A. Belov, and Y. S. Kivshar, "All-dielectric optical nanoantennas," Opt. Express **20**, 20599–20604 (2012).
12. L. Zou, W. Withayachumnankul, C. M. Shah, A. Mitchell, M. Bhaskaran, S. Sriram, and C. Fumeaux, "Dielectric resonator nanoantennas at visible frequencies," Opt. Express **21**, 1344–1352 (2013).
13. P. Albella, R. Alcaraz de la Osa, F. Moreno, and S. A. Maier, "Electric and magnetic field enhancement with ultralow heat radiation dielectric nanoantennas: considerations for surface-enhanced spectroscopies," ACS Photon. **1**, 524–529 (2014).
14. A. Krasnok, M. Tymchenko, and A. Alù, "Nonlinear metasurfaces: a paradigm shift in nonlinear optics," Mater. Today **21**, 8–21 (2018).
15. L. Carletti, A. Locatelli, D. N. Neshev, and C. De Angelis, "Shaping the radiation pattern of second-harmonic generation from AlGaAs dielectric nanoantennas," ACS Photon. **3**, 1500–1507 (2016).
16. L. Wang, S. Kruk, L. Xu, M. Rahmani, D. Smirnova, A. Solntsev, I. Kravchenko, D. Neshev, and Y. Kivshar, "Shaping the third-harmonic radiation from silicon nanodimers," Nanoscale **9**, 2201–2206 (2017).

17. L. Ghirardini, L. Carletti, V. Gili, G. Pellegrini, L. Duò, M. M. Finazzi, D. Rocco, A. Locatelli, C. De Angelis, I. Favero, M. Ravaro, G. Leo, A. A. Lemaitre, and M. Celebrano, "Polarization properties of second-harmonic generation in AlGaAs optical nanoantennas," Opt. Lett. **42**, 559–562 (2017).
18. S. S. Kruk, R. Camacho-Morales, L. Xu, M. Rahmani, D. A. Smirnova, L. Wang, H. H. Tan, C. Jagadish, D. N. Neshev, and Y. S. Kivshar, "Nonlinear optical magnetism revealed by second-harmonic generation in nanoantennas," Nano Lett. **17**, 3914–3918 (2017).
19. M. Guasoni, L. Carletti, D. N. Neshev, and C. De Angelis, "Theoretical model for pattern engineering of harmonic generation in all-dielectric nanoantennas," IEEE J. Quantum Electron. **53**, 6100205 (2017).
20. P. Albella, M. A. Poyli, M. K. Schmidt, S. A. Maier, F. Moreno, J. J. Sáenz, and J. Aizpurua, "Low-loss electric and magnetic field-enhanced spectroscopy with subwavelength silicon dimers," J. Phys. Chem. C **117**, 13573–13584 (2013).
21. U. Zywietz, M. K. Schmidt, A. B. Evlyukhin, C. Reinhardt, J. Aizpurua, and B. N. Chichkov, "Electromagnetic resonances of silicon nanoparticle dimers in the visible," ACS Photon. **2**, 913–920 (2015).
22. R. M. Bakker, D. Permyakov, Y. F. Yu, D. Markovich, R. Paniagua-Domínguez, L. Gonzaga, A. Samusev, Y. Kivshar, B. Luk'yanchuk, and A. I. Kuznetsov, "Magnetic and electric hotspots with silicon nanodimers," Nano Lett. **15**, 2137–2142 (2015).
23. S. Gehrsitz, F. K. Reinhart, C. Gourgon, N. Herres, A. Vonlanthen, and H. Sigg, "The refractive index of $Al_xGa_{1-x}As$ below the band gap: accurate determination and empirical modeling," J. Appl. Phys. **87**, 7825–7837 (2000).
24. E. E. Radescu and G. Vaman, "Exact calculation of the angular momentum loss, recoil force, and radiation intensity for an arbitrary source in terms of electric, magnetic, and toroid multipoles," Phys. Rev. E **65**, 046609 (2002).
25. A. E. Miroshnichenko, A. B. Evlyukhin, Y. Feng Yu, R. M. Bakker, A. Chipouline, A. I. Kuznetsov, B. Luk'yanchuk, B. N. Chichkov, and Y. S. Kivshar, "Nonradiating anapole modes in dielectric nanoparticles," Nat. Commun. **6**, 8069 (2015).
26. G. Grinblat, Y. Li, M. P. Nielsen, R. F. Oulton, and S. A. Maier, "Enhanced third harmonic generation in single germanium nanodisks excited at the anapole mode," Nano Lett. **16**, 4635–4640 (2016).
27. D. Bouchet, M. Mivelle, J. Proust, B. Gallas, I. Ozerov, M. F. Garcia-Parajo, A. Gulinatti, I. Rech, Y. De Wilde, N. Bonod, V. Krachmalnicoff, and S. Bidault, "Enhancement and inhibition of spontaneous photon emission by resonant silicon nanoantennas," Phys. Rev. Appl. **6**, 064016 (2016).
28. D. Rocco, L. Carletti, A. Locatelli, and C. De Angelis, "Controlling the directivity of all-dielectric nanoantennas excited by integrated quantum emitters," J. Opt. Soc. Am. B **34**, 1918–1922 (2017).
29. D. de Ceglia, M. A. Vincenti, C. De Angelis, A. Locatelli, J. W. Haus, and M. Scalora, "Role of antenna modes and field enhancement in second harmonic generation from dipole nanoantennas," Opt. Express **23**, 1715–1729 (2015).